



PUBLICATION

MUSTANG

A MULTIPLE Space and Time scale Approach for the QUANTIFICATION of deep saline formations for CO₂ STORAGE

Project Number: 227286

AUTHORS:

LINDA LUQUOT^{1*}, MURIEL ANDREANI², PHILIPPE GOUZE¹, PIERRE CAMPS¹

¹Géosciences Montpellier, Université Montpellier 2 - CNRS, Montpellier, 34095, France

²Laboratoire de Géologie de Lyon – Université Claude Bernard-Lyon1, Lyon, 69622, France

TITLE:

**CO₂ PERCOLATION EXPERIMENT THROUGH CHLORITE/ZEOLITE-RICH SANDSTONE
(PRETTY HILL FORMATION – OTWAY BASIN – AUSTRALIA)**

The research leading to these results has received funding from the European Community's Seventh Framework Programme [FP7/2007/2013] under grant agreement n° [227286]

Status	AUTHOR VERSION
Date	
Publisher	Chemical Geology
Reference	Luquot, L., Andreani, M., Gouze, Ph., and Camps, P. – CO ₂ percolation experiment through chlorite/zeolite-rich sandstone from Pretty Hill formation - Australia. Chemical Geology. doi:10.1016/j.chemgeo.2011.11.018 (2012).



Abstract.

Underground CO₂ sequestration is highly recommended as an effective means of significantly decreasing CO₂ concentration in the atmosphere. Mineral storage is the more secure technology, but requires the presence of high concentration of divalent cations in the pore-fluid. Results from CO₂ percolation experiments through chlorite/zeolite-rich sandstone samples from the Pretty Hill Formation (Otway Basin, Australia) are presented. The dissolution of the laumontite (7 wt%) and chamosite (7 wt%) are the potential sources of calcium, iron and magnesium required for carbonate precipitation. The percolation experiment was setup to reproduce, at laboratory scale, the in situ temperature and pressure conditions ($T = 95\text{ }^{\circ}\text{C}$ and $P = 10\text{ MPa}$). The fluid injected at constant flow rate is a rock-equilibrated brine subsequently enriched in CO₂ up to partial pressure of 6 MPa.

We observe feldspars, laumontite and chamosite dissolution, kaolinite and silica precipitation and a noticeable sink of CO₂ in the sample which is attributed to the precipitation of both amorphous carbon due to the reduction of CO₂ and Fe-rich carbonate. Permeability decreases of about one order of magnitude due to the localization of the kaolinite precipitation in the main flow paths, while porosity increases.

The high reactivity of this sandstone makes this reservoir a valuable target for CO₂ mineralization, but the associated permeability decrease may limit the injection rate and the spreading of the CO₂ in the reservoir.

Keywords: CO₂ storage, clay precipitation, carbon, permeability, reactive transport.



1. Introduction

Decreasing atmospheric concentration of CO₂ is one of the key challenges of this century. Geological storage of CO₂ in reservoir pore fluid, is one of the diverse technologies being explored for decreasing atmospheric concentration of CO₂ (Bachu et al., 2007; Pacala and Socolow, 2004; Lackner, 2003; Hoffert et al., 2002). Deep saline aquifers and depleted oil and gas reservoirs are valuable targets for this purpose (Bickle, 2009). Each reservoir has their own advantages: the main ones for saline aquifers are their large potential volume of storage and their common occurrence; whereas oil fields are very well known and described. After injecting the CO₂ as a supercritical fluid at depth, a certain amount will slowly dissolve into the pore water, while the rest will flow upward, driven by buoyancy forces (Gunter et al., 2004). However, supercritical or gaseous CO₂ can be trapped for very long periods (several hundreds of years as in natural CO₂ reservoir storage, *Ballentine et al., 2001*) below the confining layers because of the slow dissolution kinetic triggered by the thermodynamic laws and the limited mixing between the CO₂ and the brine. Confining layers are the ultimate seals to ensure that the stored CO₂ does not return to the atmosphere and any hydraulic discontinuity produced or reactivated by the injection itself or tectonic events may cause the depressurized of the CO₂-brine mixture, pressure gradients (augmented by the exsolving of the dissolved CO₂) and eventually the upward flow of supercritical or gaseous CO₂ accompanied by caprock chemical alteration (e.g. Rochelle et al., 2004; Andreani et al., 2008). Then, assuming that storage capacity is sufficient to warrant the development of the technologies for geological sequestration of CO₂ in pore fluid, it raises major issues for long term safety (risk of CO₂ leakage to other overlying aquifers exploited for drinking water or to the surface due to containment failures) and consequently public acceptance (e.g. Hawkins, 2004; Damen et al., 2006). Conversely, CO₂ geo-mineralization is



a potential alternative solution for long lasting, thermodynamically stable and environmentally safe sequestration of CO₂ (Baines and Worden, 2004; Xu et al., 2004; Oelkers et al., 2008; Goldberg and Slagle, 2009; Matter et al., 2007; Andreani et al., 2009; Daval et al., 2009; Hangx and Spiers, 2009; O'Connor et al., 2004; Matter and Kelemen, 2009). This technique consists in converting CO₂ to solid magnesium, calcium or iron carbonate while dissolving Mg-, Ca-, Fe-rich silicates. In this case, it is expected that both the kinetic barriers and (partially) irreversible fluid-rock reactions will prevent CO₂ returning to the atmosphere. Until now, experimental and numerical investigations into mineral trapping have focused on Mg-Ca-rich minerals such as olivine or wollastonite (Andreani et al., 2009; Daval et al., 2009; Kelemen and Matter, 2008), but only few studies have been dedicated to reactions involving Fe-rich minerals at pressure and temperature representative of CO₂ injection conditions (i.e. $8 < P < 20$ MPa and $50 < T < 150^{\circ}\text{C}$) (Palandri et al., 2005; Wigand et al., 2008).

This contribution aims at studying the geochemical and hydrodynamic changes induced by massive injection of CO₂ into the chlorite/zeolite-rich sandstone, known as the Pretty Hill formation, of the Katnook reservoir, (Otway Basin Australia). The Katnook reservoir is formed of Si-rich minerals containing divalent cation such as chamosite and laumontite which can induce carbonate precipitation and thus CO₂ mineral storage. This reservoir contains less than 1 mol% CO₂). Conversely, the Otway Basin contains numerous CO₂-rich gas accumulations that are being studied as natural analogues for the geological storage of CO₂ (Watson et al., 2003). In particular, the Ladbroke Grove reservoir, an area of the pretty Hill formation compartmented by impermeable faults, displays CO₂ accumulation due to past volcanic events. Consequently, Ladbroke Grove reservoir can be used for comparison with the experimental results.



To explore the reaction processes occurring in Fe-rich geological reservoirs, while reproducing the conditions for CO₂ injection and storage in geological formations, we developed a flow-through-rock experimental apparatus. Unlike standard experiments realised in closed static or flushed vessels, flow-through experiments can reproduce the continuous disequilibrium induced by renewal of reactants at the reaction surfaces. For such highly reactive systems, the heterogeneity of the flow field at sub-micron to micron-scale can initiate chemical microenvironments, where the fluid composition differs from the bulk composition in the vicinity of the mineral interfaces (Andreani et al., 2009 and Steefel et al., 2005). The occurrence of these microenvironments, where dissolution and precipitation can take place, is controlled by the distribution of diffusive and advective zones triggered by the heterogeneity pore network structure and the spatial distribution of the minerals.

In the following we will report the results based on two reproducible CO₂-rich brine percolation lab-scale experiments reproducing in situ reservoir conditions at the Katnook Pretty Hill formation (i.e. $T = 95^{\circ}\text{C}$ and $P = 10 \text{ MPa}$). These experiments were realized in the same conditions to repeatability. These experiments allow us to study the relationship between the time-resolved changes of the rock composition, porosity and permeability induced by the mass transfers during the percolation. The methodology combines chemical analysis of the fluid, continuous measurements of sample permeability, and pore-scale characterisation of the rock by ESEM and TEM analysis.

2. Geological setting and reservoir petrography

The Otway Basin is an NW-SE extensional basin that developed along the southern margin of eastern Australia in association with the separation of



Australia from Antarctica (Perincek and Cockshell, 1995). Early Cretaceous and possibly Late Jurassic fluvial and lacustrine sediments were deposited in fault-bounded depocentres (Parker, 1992). The Ladbroke Grove and Katnook reservoirs, studied here, are located within the Penola Trough of western Otway Basin in Pretty Hill Formation (Fig. 1A) and they are separated by the Ladbroke Grove fault (Fig. 1B). This formation comprises well sorted, fine to medium-grained, lithic-rich sandstones and minor interbedded siltstones (Kopsen and Scholefield, 1990).

The siliciclastic gas reservoir at Ladbroke Grove contains high levels of CO₂ (from 26 mol % up to 57 mol % CO₂) provided by the recent volcanic activity (<1 Ma) within the region and local hydrothermal intrusions (Chivas et al., 1987; Giggenbach et al., 1991) which migrated into the methane accumulation. The latest events took place in the Mount Gambier (Fig.1A) area around 4500 years ago (Sheard, 1995). In opposition, one kilometre away at a similar depth but on the other side of the impermeable Ladbroke Grove fault, the Katnook reservoir contains methane but less than 1 mol % CO₂ (Watson et al. 2003). This difference in CO₂ levels within the same formation, reflecting recent contrasting CO₂ influx within these two reservoirs, makes the Ladbroke Grove and Katnook reservoirs excellent analogues for the studying CO₂ – sandstone reactions (Watson et al., 2003), but is also useful means for validating the laboratory experiments.

The reservoirs of Katnook are little evolved (acicular), with fine to medium-grained feldspathic to lithic sandstones (Watson et al., 2003). These rocks are composed of minerals from various origins: granitic, metamorphic and volcanic. Late hydrothermal circulations are testified by the presence of laumontite (zeolite). The mineralogy of Katnook is quite complex, with volcanic lithic rock fragments (trachyte fragments), angular to sub-rounded quartz grains, K-feldspar (sometimes a little altered), sodium-rich plagioclase, iron-rich chlorite



and laumontite (Fig. 2). The bulk chemical composition of the trachyte fragments is similar to the one of feldspars grains (microcline and albite). An iron rich chlorite (chamosite) is observed on the surface of most of the grains, in particular around the fragments of volcanic rock. The cement of the sandstones mainly consists of calcite and/or laumontite. Other accessory minerals (in very small proportion < 2-3%) can also be observed depending on the depths, such as garnets, muscovite or titanite.

Ladbroke Grove reservoir (initially displaying the same composition as Katnook, Watson et al., 2004) presents evidences of interactions with CO₂. New minerals appear at the expense of initial ones. The presence of kaolinite is observed as a replacement feldspars and chamosite. The formation of ferrous carbonates (siderite, ankerite) participated in the replacement of the chamosite. The cement (calcite and/or laumontite) is dissolved and replaced by dolomite (more or less ferrous).

Porosity and permeability measurements of Katnook and Ladbroke reservoir have been realized by Watson et al. (2003) and are available in well completion reports. The average porosity of Katnook reservoir ranges from 8 to 15 % depending on the depth. The porosity at Ladbroke Grove is quite similar despite its strong geochemical difference, and ranges between 6 and 19 %. The permeability at Ladbroke Grove and Katnook ranges from 44.7 to 52 mD and from 28 to 42.1 mD respectively.

3. Experimental Methodology and Sample Properties.

We realized two flow-through experiments through two Katnook samples (KAT1 and KAT2). These two experiments were realized under the same



conditions to test reproducibility. The experiments involve injecting CO₂-enriched brine (of known composition) at constant flow rate through cylindrical cores of 9 mm diameter (D) and 18 mm length (L). These experiments were realized using the flow-through apparatus ICARE 2 (Fig. 3), which allows reproducing the in-situ reservoir conditions for CO₂ sequestration.

Flow-through experimental equipment

The flow-through apparatus ICARE 2 (Fig. 3) allows reproducing the in-situ reservoir conditions for CO₂ sequestration ($T < 200^{\circ}\text{C}$ and $P < 20 \text{ MPa}$). It is composed by two motorised piston pumps (made in hastelloy-C22), one for the injection and the other one for the backpressure control. The two pumps are equipped with displacement encoders, which allow an accurate control of the flow rate (fluctuations $\leq 0.01 \text{ cm}^3/\text{h}$). In the percolation cell, radial confining pressure is applied to the silicon jacket covering the sample. The confining pressure is maintained at 117% of the inlet pressure. This system is essential for minimising stresses on the sample during pressure and temperature loading and unloading at the beginning and the end of the experiment. To achieve this objective, we used a pressure multiplier with a free-moving piston of dissymmetric diameter.

Permeability is recorded continuously by measuring the pressure drop between the inlet and outlet sample (using a differential pressure sensor Rosemount 3051) and using the Darcy's law, which stipulates that, for laminar flow, permeability (in m^2) scales linearly with the ratio of the volumetric flow rate Q (in $\text{m}^3 \cdot \text{s}^{-1}$) over the pressure difference ΔP (in Pa): $k = \mu L Q / S \Delta P$ where L is the length of the sample (in m) in the flow direction, S is the cross-sectional area of the sample (in m^2), and μ is the dynamic viscosity of the brine (in Pa.s).

We developed two specific micro-sampling tools with a total volume of 0.3 and 2 cm^3 for sampling CO₂-saturated brine under the experimental pressure condition.



Using the smaller one, we applied the following method to evaluate the CO₂ concentration: (1) cooling of the sampled fluid volume at experimental pressure condition, (2) decompression of the fluid, inducing CO₂ degassing into the micro-sampler, (3) measure of the total volume at atmospheric pressure of the brine + CO₂ by flushing these fluids in a graduated test-tube (4) calculation of the CO₂ fraction knowing the CO₂ solubility in the brine at atmospheric pressure and room temperature.

Analytical methods

Outlet waters are analyzed for concentrations of Si, Ca, Mg, Al, K and Fe using Inductively Coupled Plasma-Atomic Emission Spectrophotometry (for cations concentrations) (ICP-AES). Reaction progress and porosity changes are calculated from the mass balance between injected and effluent waters, applying the chemical composition of the rock.

As a general rule, core samples are characterized before and after experiments to observe and quantify the changes due to fluid-rock interactions. For invasive measurements, samples are taken just beside the core from the remaining rock volume after coring. All the analyses were realized on a Representative Elementary Volume (REV) of 1 cm³. The mineralogy of the two core samples was characterized in details using petrographic microscopy, quantitative X-Ray Diffraction (XRD) and X-Ray Fluorescence (XRF). Bulk rock analysis using carbon analyzer Leco SC144 DRPC was performed for quantifying TOC (Total Organic Carbon) and TCC (Total Carbon Content). Mossbauer technique allowed estimating the iron oxidation state in the chamosite mineral. Mossbauer spectrum was collected on a conventional constant-acceleration spectrometer. A ⁵⁷Co source in Rh matrix with an activity of about 10 mCi was used. Velocity calibration was obtained with iron foil as a reference absorber.



We used the Electron Probe MicroAnalysis (EPMA, CAMECA SX100) to determine the minerals composition and calculate the structural formula of each individual mineral phases (see table 1).

The detailed characterization of sample after experiment was realized down to nano-scale using Environmental Scanning (ESEM) and Transmission (AEM/TEM) Electron Microscopes. ESEM was performed under low vacuum mode (with 70.7 Pa of water pressure) with a FEI Quanta 200 instrument equipped with a field emission gun and a dispersive X-ray system. TEM characterization and nano-analyses were performed with a JEOL 2010F high-resolution transmission electron microscope working under a 200 kV acceleration available at the CLYM (Lyon, France). This TEM is equipped with an Energy Dispersive Spectrometer (EDS-TEM) for major element analyses on circular area of about 30 nm in diameter in fixed-beam mode.

Raman spectra of carbon were collected in a back-scattering geometry with a LabRAM ARAMIS Raman spectrometer on volume of $\sim 2 \mu\text{m}^3$. The exciting radiation ($\lambda = 473 \text{ nm}$) was provided by a He/Ne laser focused on the sample using an optical microscope ($\times 50$ objective).

Magnetic measurements were performed using a cryostat apparatus (CS-L) and a furnace (CS-3) under Ar atmosphere coupled to the KLY-3 Kappabridge instrument. We used the method of Prévot et al., (1983) to estimate the mean Curie temperature of magnetic mineral revealed by a reversible fall in the K - T curves.

Sample composition

The rock sample used for the experiments was provided by PIRSA (Primary Industries and Resources South Australia) and comes from the Katnook reservoir (Well 3, 2924.25 m depth). Thanks to the previous mineralogical and



petrographical descriptions given by PIRSA, the rock sample was selected with high zeolite content and without calcite in order to clearly identify the potential precipitation of new carbonates. Two cylinders (KAT1 and KAT2, 9 mm diameter (D) and 18 mm length (L)) were cored side-by-side in the rock sample and display similar properties, the objective being to verify the reproducibility of the experiment.

The two samples have the same composition and are quartz-rich (44%) with 13% potassium feldspar (microcline), 29% sodium feldspar (albite), 7% zeolite (laumontite), 7% Fe-chlorite (chamosite) and 0% carbonate. About 14% of the grains consist of volcanic rock fragments with mineralogy similar to the whole feldspar. Mossbauer measurements indicate that the chamosite is composed by 22.3% of Fe^{3+} and 77.7% of Fe^{2+} . Bulk rock analysis indicate that the initial sample contains 0.107 ± 0.005 wt.% total carbon and 0.0259 ± 0.0004 wt.% organic carbon.

Experimental conditions

The two consisted in injecting CO_2 -enriched brine at constant flow rate through the cores using the same experimental conditions. They were carried out at total pressure $P = 10 \pm 0.3$ MPa, temperature $T = 95 \pm 0.4^\circ\text{C}$, i.e. the pressure and temperature conditions of Ladbroke Grove reservoir (see Kirste et al., 2004). The CO_2 partial pressure (P_{CO_2}) of the inlet brine is set to 6 MPa (i.e. 0.402 mol/l of CO_2), and obtained by mixing rock-equilibrated brine and industrial-grade pure CO_2 . The rock-equilibrated brine was made using deionized water and laboratory grade salts in order to reproduce pore fluid measured in the Pretty Hill Formation (Watson et al., 2003). Its chemical composition is reported in table 2 (the pH is calculated using the geochemical code Phreeqc; Parkhurst, 1995). The Si, Mg, Ca, Fe, K and Al concentration in the fluid samples at the inlet



and the outlet of percolation cell, as well as in the deionised rinsing waters, were analyzed using Inductively Coupled Plasma-Atomic Emission Spectrophotometry (ICP-AES). CO₂-enriched brine was injected at constant flow rate $Q = 0.3 \pm 0.01$ cm³/h for the both experiments. The duration of the experiments was 118 hours and 157 hours for KAT1 and KAT2, respectively.

The permeability of KAT1 and KAT2, measured before the CO₂-rich brine injection during brine water Pretty Hill reservoir injection, was $(1.37 \pm 0.13) \times 10^{-15}$ m² and $(1.48 \pm 0.09) \times 10^{-15}$ m² (i.e. 1.37 and 1.48 mD), respectively. The initial porosity, measured by X-ray microtomography images (pixel size 5.06 μm), was 11.2 ± 0.3 % and 10.9 ± 0.2 %, respectively.

4. Results and discussions

The two experiments produced similar changes in permeability (Fig. 4) and similar outlet brine chemistry, emphasizing the reproducibility of the experiment. The permeability decreases significantly from $(1.37 \pm 0.13) \times 10^{-15}$ m² to $(1.04 \pm 0.08) \times 10^{-16}$ m² for KAT1 after 118 hours of seawater percolation and from $(1.48 \pm 0.09) \times 10^{-15}$ m² to $(8.78 \pm 0.06) \times 10^{-17}$ m² for KAT2 after 157 hours of seawater percolation. For simplicity, the chemical results (Fig. 5) are illustrated only for the longest experiment (experiment KAT2, chemical results for experiment KAT1 are available as supplementary data).

The recurrent fluid analyses provide a record of the geochemical reactions between CO₂, brine and the Katnook sandstone. The fluid sampling started 12 h after the injection of the CO₂-rich brine starts. Temporal changes in the major elements are shown in Fig. 5. Because of the low injection rate ($Q = 0.3 \pm 0.01$ cm³/h), no sampling was made between $t = 0$ and $t = 12$ h to have enough percolated fluid for chemical analyses (at least 3ml are needed for cation



measurements), thus, the concentration changes are unknown during this period. From the observation of the decrease trend of the concentration curves for $t < 60$ h, it can be expected that at $t = 20$ min (fluid residence time), the concentrations were higher than at $t = 12$ h. This unmeasured part of the curve was not accounted for in the mass balance calculations. Consequently, the mass balance calculations discussed in the following of this paper represent minimum values of dissolve and precipitate mineral. In the following we will first discuss the dissolution and precipitation reactions (sections 4.1 and 4.2), then the mass balance accounting for dissolution and precipitation will be established (section 4.3).

4.1 Identification of the dissolution reactions

Bulk quantitative analysis of the samples after the percolation experiment using XRD and X-Ray fluorescence indicates a massive decrease of the laumontite, microcline and albite content (table 3). This is in accordance with the micrographs (Figs. 6A and B) which show that feldspar crystals are strongly altered after the CO₂-rich brine percolation (Fig. 6B). Chamosite and laumontite also show dissolution patterns (Fig. 6A), principally along the cleavage planes for the latter.

Concentration change with time ($\Delta C_i = C_i|_{out} - C_i|_{in}$, with $i = \text{Si, Ca, Mg, Al, K and Fe}$) are positive during the experiment (Fig. 5) and confirms the progressive dissolution of minerals. According to the initial EPMA analyses of the rock forming minerals, the release of Si, Ca, Mg, Al, K and Fe can be related to chamosite, laumontite and feldspar dissolution. The release of Ca can only be attributed to the dissolution of laumontite, whereas the release of Mg and Fe is due to chamosite dissolution (see table 1). The Ca concentration in the outlet fluid relative to other laumontite-forming cations is higher than the expected one



for a stoichiometric dissolution of laumontite for $t < 30$ hours. Two hypothesis can explain this high Ca concentration. A non-stoichiometric dissolution was already observed by Savage et al. (1993) but at high pH (8 – 10) but this mechanisms can not be directly extrapolated to our low pH conditions. The second, most probable, alternative is a stoichiometric dissolution coupled with a precipitation of Si and Al rich-minerals and a release of Ca in the outlet fluid.

For $t > 30$ hours, the Mg concentration in the outlet fluid becomes the highest one. Mg concentration indicates chamosite dissolution which, as for laumontite, represents only 7% of the rock-forming minerals. The difference between the Ca and Mg concentrations in the outlet fluid can be related to the high relative surface area of chamosite (sheet structure) compared to laumontite. Yet, the interpretation of the outlet fluid composition (Fig. 5) requires the direct observations of the precipitated minerals and mass balance calculations.

4.2 Identification of the Precipitation reactions

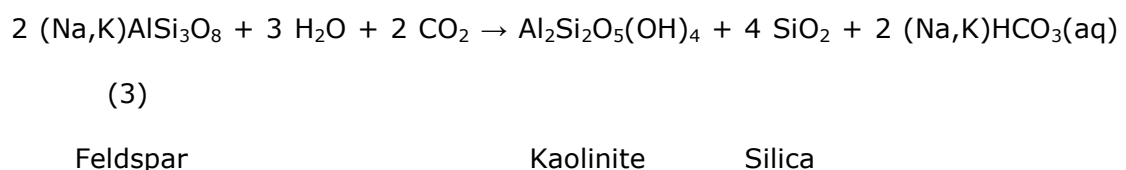
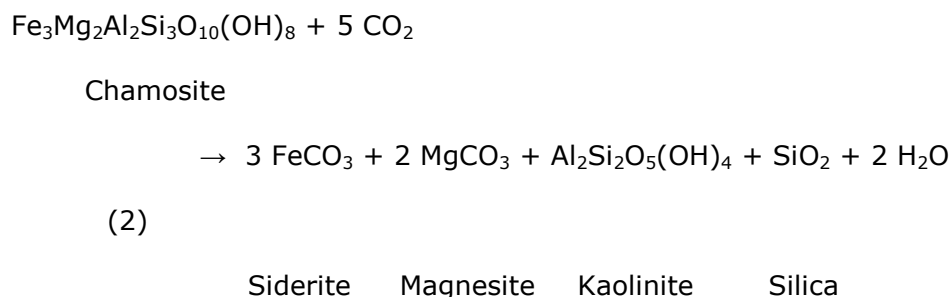
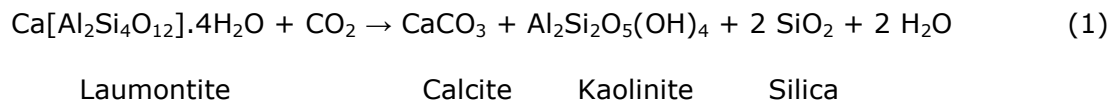
We observe that the Si concentration is very low compared to the others concentrations in spite of the high proportion of Si in the dissolved minerals. XRD and X-Ray fluorescence observation show a higher amount of quartz after experiment than that observed before the experiments (table 3). This is in accordance with the micrographs (Figs. 6B) which show that quartz grains remain unaltered.

Using the Si concentration in the outlet fluid, we calculate the equivalent $\text{SiO}_{2(\text{aq})}$ concentration. Dissolved silica concentration decreases from 74.25 to 41.06 mg/l during the experiment. At the temperature of the experiment, quartz saturation is theoretically about 48 mg/l $\text{SiO}_{2(\text{aq})}$, so that the outlet fluid is over-saturated with respect to quartz during a long period of the experiment.



Consequently, quartz or other forms of silica minerals precipitation, is expected to occur.

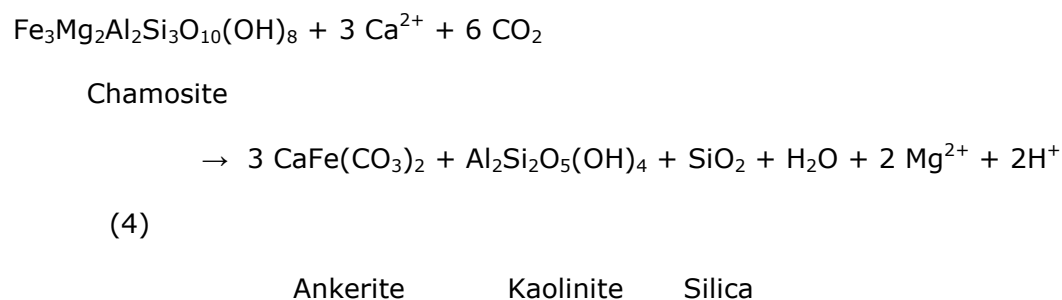
X-ray analyses also reveal a more important fraction of chamosite after experiment (table 3), in opposition to ESEM observation (Fig. 6) and to the significant release of Fe and Mg in the outlet fluid (Fig. 5). However, according to the difficulty to distinguish small fractions of sheet silicates using bulk powder XRD, we can reasonably propose that an important part of the supposed chamosite measured by XRD is kaolinite which was clearly identified to be precipitated on feldspar surfaces (Fig. 8) and on laumontite cleavage plane (Fig. 7). This is also corroborated by the outlet fluid data, depleted in Si and Al, and the previous observations realized by other authors; kaolinite and quartz have been previously identified as products of the reaction with CO₂-rich fluids (Figs. 8A, 8B and 7) during the batch experiments published by Kirste et al. (2004) and Ketzer et al. (2009). The corresponding reactions are those given as follow (Eqs. (1), (2) and (3)):





Others authors reported strong feldspar dissolution coupled with clay and quartz precipitation in presence of high CO₂ concentration and underground storage temperature conditions during laboratory experiments (e.g. Kaszuba et al., 2003; Wigand et al., 2008; Rosenbauer et al., 2005; Druckenmiller and Maroto-Valer, 2005 and Kirste et al., 2004), numerical modeling (e.g. Xu et al., 2004; Zerai et al., 2006 and Ketzer et al., 2009) and by natural analogues observations (e.g. Wilkinson et al., 2009).

The concentration of Mg and Fe do not display the stoichiometric ratio expected during the dissolution of chamosite (Fe₃Mg₂Al₂Si₃O₁₀(OH)₈). The ratio Mg:Fe as well Fe:Si and Mg:Si indicate that Fe and to a lesser extent Mg are retained in the samples. Kirste et al. (2004) published the results of batch experiments performed at the same temperature and pressure conditions as for our experiments, using the same fluid compositions and samples from Katnook reservoir. These authors (*op.cit.*) observed carbonate precipitation, for instance ankerite (Ca(Fe,Mg)(CO₃)₂), and proposed the following reaction:



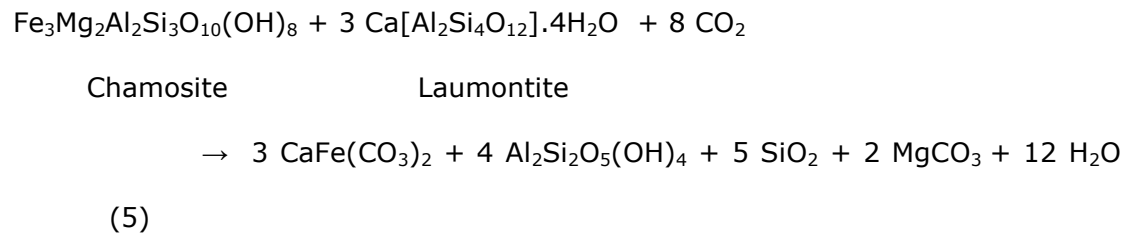
Conversely, long duration batch experiments (~2.5 months) performed by Kaszuba et al. (2003, 2005) have shown that carbonate (magnesite and siderite) precipitation occurs in sandstone shale systems, at 200°C and 20 MPa total pressure, together with secondary phases (e.g. smectite clays and quartz). For our experiment, carbonate precipitation was not directly observed by ESEM



images or measured by XRD, but the CO_2 concentration variation (ΔC_{CO_2}) is negative (Fig. 5) and indicates that CO_2 is stored into the sample. The measurement of the total and organic carbon after experiment indicate that both carbonate minerals and organic carbon have precipitated during the percolation experiment. We measure a total carbon content (TC) of 0.195 ± 0.005 wt.% and organic composition (TOC) of 0.0855 ± 0.0006 wt.% in the reacted sample. By comparison to our initial measurements, realized before experiment, (TC = 0.107 ± 0.005 wt.% ; TOC = 0.0259 ± 0.0004 wt.%), the total carbon concentration increases considerably (82% of increase). This increase corresponds mainly to an increase in organic carbon (67% of the total increase) and a lower increase in inorganic carbon, i.e. carbonate precipitation. Indeed, the simultaneous formation of both carbonate mineral(s) and C^0 within the sample demonstrates that different isolated microenvironments may develop. Thermodynamical calculations (using EQ3NR data base; Wolery, 1992) indicate that Fe-carbonates and Fe-oxides can precipitate for the temperature and pressure under consideration and in the experimental pH range (3.9 for inlet fluid to 5.21 for the outlet fluid, calculated using the Phreeq-C program). The pE-pH diagram (Fig. 9) shows that carbonate precipitation may occur only in a restricted range of pH and pE. Yet, as mentioned above, fluid composition can be very heterogeneous at pore scale due to the spatial variability of the driving processes that control solute transport (diffusion versus advection) and mass transfer (solute transport versus reaction rate) in the vicinity of the reactive surfaces. The result is that sample scale averaged values for pH and pE cannot be used for predicting the actual reaction paths. But the post-experiment analysis of the rock-forming mineral can be used to identify the dissolved and precipitated phases. As mentioned above, the precipitation of carbonate was not directly observed by microscopy techniques; however it is indirectly detected by the increase of inorganic fraction of the total



carbon in the sample. It is probable that carbonates co-precipitate as disseminated particles with kaolinite near the laumontite or into the laumontite cleavage or near the chamosite as described by Eqs. (1), (2) and (4) and the following reaction (Watson et al., 2003 and Kirste et al., 2004):



Ankerite Kaolinite Quartz Magnesite

As the results of similar experiments Kirste et al. (2004) observed siderite and ankerite precipitation. They also observed iron oxide near the dissolved chamosite. Thermodynamical modelling (Fig. 9) indicates that iron-oxide can precipitated during our experiments. TEM observation of the reacted samples (Fig. 10) reveals the precipitation of < 5 nm grains of Fe-rich minerals that are free of carbon. These phases are systematically observed close to the chamosite. Low temperature K-T curves (Fig. 11) indicate that before experiment the rock did not contain any magnetic minerals, whereas the rock contains nanoscale magnetic minerals after experiment. Moreover, the high temperature K-T curves show that these magnetic minerals are mostly magnetite (mean Curie temperature of 582 °C, Prévot et al., 1983). TEM-EDS data suggest that these magnetite grains may be surrounded by an amorphous material made of almost pure carbon (Fig. 10). Micro-Raman spectroscopy reinforces this hypothesis in chamosite-rich zones where the presence of carbon clusters formed by disordered poorly crystalline graphite (Fig. 10) are observed. Indeed, the highly disordered structure of the C phase is responsible for the larger D and G bands of carbon.

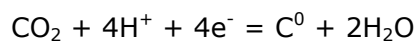


As described in Eq. 6, the iron oxidation releases electrons, causing locally a more reduced environment, which in turn can allow the CO₂ reduction following the reaction of Eq. 7.

The coupled redox equations characterising the proposed concomitant Fe oxidation and CO₂ reduction are:

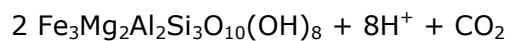


(6)

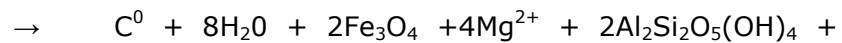


(7)

Using the information described above, the dissolution reaction of chamosite can be modelled by the following reaction:



Chamosite



2SiO₂ (8)

Graphite

Magnetite

Kaolinite

Silica

The decrease of the value of $|\Delta C_{\text{CO}_2}|$ with time follows the decrease of the corresponding ratios Mg:Fe and Fe:Si. Consequently, the iron precipitation is directly linked to the carbon precipitation, either as Fe-rich carbonates (such as ankerite or siderite) or as magnetite and reduce carbon depending on the microenvironment properties (Andreani et al., 2009). Near chamosite dissolution, we observe Fe²⁺ oxidation coupled with CO₂ reduction into C, while the precipitation of ankerite is expected near laumontite were Ca concentration is higher.

4.3 Mass Balance Calculation



Knowing the mineral composition of the rock sample and the structural formula (see table 1) of each of the initial and produced minerals, the progress of the reaction can be determined from mass balance calculations using both the inlet and the outlet composition of the brine. The mass balance is performed as the following. First, we state that the changes of Ca concentration in the fluid are due to laumontite dissolution only and assume that calcite is not produced during the experiment. Second, we assume that the Mg concentration is controlled by the chamosite dissolution. Third, the mass of dissolved microcline is estimated using the K concentration while the dissolved albite is not evaluated during the experiment because of the lack of Na concentration information (the high concentration of Na in the inlet brine preventing measuring small changes). Following these assumptions we can calculate the mass and reaction rate of the dissolved and precipitated minerals using the Si, Mg, Ca, Fe, K, and Al breakthrough curves (Fig. 5). We recall that the mass of dissolved albite, if any, is not accounted for and consequently the total mass of dissolved minerals may be under-estimated.

To calculate the total mass of reaction products we set the carbon as reduce carbon and siderite in the proportion calculated at the end of the experience by TOC and TCC. Consequently, we distributed the iron precipitation into siderite and magnetite with the corresponding stoichiometric contents. Calculations have been done for all the products independently, in order to estimate end-member mass balance. The total mass of the reaction products (kaolinite + silica + carbon + magnetite + siderite) is calculated, attributing the deficit in Fe in the outlet brine to the precipitation of magnetite and siderite, as specified above. Then the kaolinite precipitation is determined by the Al concentration and the deficit in Si in the outlet brine is compensated by silicate precipitation.



The total mass of dissolved phases (microcline + chamosite + laumontite) integrated over the whole experiment is 60.18 mg (32.96 mg chamosite + 21.29 mg laumontite + 5.93 mg microcline), which corresponds to a volume V_d of 22.13 mm³. The total mass of precipitated minerals is evaluated to be 49.79 mg (39.41 mg kaolinite + 1.51 mg silica + 4.46 mg magnetite + 0.32 mg carbon + 4.09 mg siderite), which corresponds to a volume V_p of 17.72 mm³. We use the density of graphite for estimating the quantity of precipitated carbon. Consequently, the calculated volume of carbon can be under-estimated.

4.4. Consequences on the hydrodynamic properties

Figure 4 shows the permeability change with time for the duration of experiments KAT1 and KAT2. The permeability decreases significantly from 1.48 mD to 0.0878 mD. We observe that the permeability decreases strongly for $t < 60$ h and then display a lower decrease for $t > 60$ h. This trend mimics the concentrations breakthrough (Fig. 5). Recalling that both the flow rate Q and the inlet fluid chemistry are set constant, two reasons can explain the strong concentrations decrease for $t < 60$ h: (1) the mass transfers decreases triggered by the decrease of the reactive surface area, (2) the mineral surface accessibility decline drops due to the clay coating, as observed on Figs 7 and 8. Yet, mass transfers are important for $t > 60$ h. Figure 12 shows the total dissolved and precipitated minerals versus time. Both the volume of dissolved mineral $V_d(t)$ and precipitated minerals $V_p(t)$ increases with time for the entire duration of the experiment, the volume of precipitated minerals being always lower than that of dissolved minerals. The total volume change, $\Delta V = \int_{t=0}^{t=t_{\max}} \delta V(t) dt = -4.41 \text{ mm}^3$, with $\delta V(t) = V_p(t) - V_d(t)$, denoting an increase of porosity. For $t > 60$ h, the increase of both



$V_d(t)$ and $V_p(t)$ is almost linear and the value of $\delta V(t)$ decreases, suggesting the occurrence of a quasi-stationary volume change.

Whereas porosity increases, permeability decreases, due probably to the precipitation of sheeted, throat-blocking mineral such as kaolinite which is massively produced during the experiment (Fig. 13), and to a lesser extend microporous material (amorphous carbon, Fig. 10).

Figure 14 proposes an illustration of the kaolinite precipitation mechanism that is believed to control dissolution rates and permeability. The acidic brine reacts with chamosite, albite, laumontite and microcline minerals as demonstrated in the previous section. The localised dissolution induces pH increase and pE changes and thus allows the precipitation of kaolinite, silicate and carbonate minerals and/or oxides and carbon. In Fig. 7, we clearly observe that the kaolinite has precipitated along the laumontite cleavage planes. The local precipitation of these minerals at the interface of dissolving minerals or in cleavages decreases the accessibility of the fluid to the reactive surface area. The direct consequence is the decrease of the dissolution rate of the initial minerals and thus the decrease of the cation concentration in the outlet fluid as well as the decrease of the hydraulic radius and the increase of the flow path tortuosity: permeability decreases (Gouze and Luquot, 2011).

4.5. Comparison with natural analogue

Watson et al (2003) established the mineralogical changes to the Pretty Hill Formation in the Ladbroke Grove field through the petrological identification of CO₂-mineral reactants and products. They combined the mineralogical study with the findings from the formation water chemistry and determined the reaction processes involved with the presence of CO₂. They identified as major CO₂-



reactants, sodium plagioclase, volcanic rock fragments, chlorite and calcite or laumontite (depending on the depth). During our experiments, we characterized the same CO₂-reactant minerals. Watson et al (2003) demonstrated that the main minerals products of CO₂-reactions in Ladbroke Grove field are quartz, kaolinite and Fe-rich carbonates (see Fig. 7d in Watson et al., 2003). Also, they noticed that kaolinite has directly replaced the chlorite in the presence of CO₂, as our results we suggested as well. Moreover, they observed that quartz precipitated as small nodules, embedded in the precipitated kaolinite, and that the porosity in Ladbroke Grove is slightly increased, similarly to what we observed in our experiments (Fig. 8). However, Watson et al (2003) demonstrated that the permeability has been slightly modified, with supposed a small increase in the Ladbroke Grove Field (averaging 44.7 mD compared to 42.1 mD for the Katnook Field), whereas permeability decreases noticeably in the course of our experiment. The authors (op.cit.) suggested that precipitation and dissolution appear to be balanced because Ladbroke Grove is a closed system. Moreover, we may conjecture that such a natural system is characterized by low flow rates and low chemical gradients, while our experiment that mimic CO₂ injection in the vicinity of the injection well is characterized by a high flow rates and an high chemical disequilibrium. For instance, if we suppose a monophasique injection at 150 m³ per day as in Sleipner (Chadwick et al, 2009), an injection thickness of 8 m as suggested by Bickle et al. (2007), a rock porosity of 11% as in Katnook reservoir and a local velocity of 376 m.y⁻¹ (as forced during our experiment), we can calculate that reactions observed during our experiment are representative of what would occur at around 18 m from the injection well. Whereas, if we suppose a reservoir permeability of 50 mD (as measure by Watson et al 2004) and a classical head gradient in a sedimentary reservoir of 0.02 (de Marsilly, 1981), we can estimate that in a natural sedimentary basin



without any anthropic injection the local velocity is around 5 mm/year. These calculations indicate that in our experiment the flow rate is about 70000 times (i.e. roughly 4 to 5 orders of magnitude) higher than in natural systems without injection. As a consequence, during industrial injection we are expecting much more localisation of the reactions (Luquot and Gouze, 2009) triggered by the kinetic-controlled dissolution of the initial rock-forming mineral and by the occurrence of chemical microenvironments (Steefel et al., 2005) favouring, for instance, the local precipitation of kaolinite.

5. Conclusions

The two percolation experiments setup for reproducing in situ reservoir conditions during CO₂ injection, provide new information on reactive mechanisms between CO₂-rich brine and chlorite/zeolite-rich sandstone. It is showed that the Katnook sandstone from Otway basin strongly reacts during the CO₂-rich brine. Minerals such as feldspar, chamosite and laumontite are dissolved and the precipitation of kaolinite and silica is observed. Carbon storage is also recorded as the formation of Fe/Ca-rich carbonate minerals (ankerite, siderite) and as amorphous carbon precipitation coupled with Fe-oxyde. These results testify that CO₂ can be efficiently stored in such sandstone reservoirs and show that amorphous carbon must be considered as a possible means for storing carbon in such Fe-rich reservoirs. The detailed characterization of those amorphous phases now needs to be investigated to evaluate its stability with time; notably in comparison to the high durability of carbonate minerals

The high reactivity of this sandstone makes this reservoir a valuable target for CO₂ mineralization, but hydrated minerals precipitation such as kaolinite induces permeability decrease. This may hinder the reactive surface accessibility and may also limit the injection rate and the spreading of the CO₂ in the



reservoir. However, the efficiency of this process appears to be highly sensitive to small changes in local parameters: the initial structural and mineralogical heterogeneities, the fluid composition and, in first instance, the spatial distribution of the fluid velocity at pore scale. Beside the issues concerning caprock sealing integrity and storage safety, a successful storage requires a precise evaluation of the effective reservoir capacity and of the rate at which it can be filled (CO₂ injection performance). The effective capacity, i.e the volume fraction of the rock available for CO₂ storage, can be very different from that calculated based on the CO₂ solubility and porosity. The heterogeneity of the hydrodynamic properties and its possible changes during the injection and storage periods must be assessed, particularly in term of clay precipitation (Matthews et al. 1996). Whereas hydrodynamic heterogeneity main enhance the mixing of CO₂ with the brine, increasing the solubility rate and the spreading of the CO₂-brine mixture (Hovorka et al., 2004), local decreases of the permeability may create large zones unavailable for storage. Moreover, permeability decrease induced, for instance, by clay precipitation and fine clay particles transport in the vicinity of the CO₂ injector well may eventually slow down injection and downgrade the injection performance to a point that it becomes no more pertinent in terms of economical and environment objectives.

In conclusion, carbonation is observed during these experiments and is always highly localized. The reason is that the heterogeneous spatial distribution of mixing, triggered by the variability of the velocity field in pores, promotes the development of chemical microenvironments where the fluid composition is different from the bulk concentrations. It follows that the occurrence and the rate of reactions cannot be tackled by standard effective models, and it is presently difficult to conclude on the efficiency and the sustainability of in situ CO₂ sequestration via carbonation. Nevertheless, it is clear that the injection rate is an



important parameter that will control both carbonation mechanisms and permeability changes.

Acknowledgements

This work was supported by TOTAL S.A. and by the 'MUSTANG' project (European Community FP7/2007-2013 under grant agreement n°227286). These sources of funding are gratefully acknowledged. We also want to thank the Primary Industries and Resources South Australia agency (PIRSA, <http://www.pir.sa.gov.au/>) for allowing us sampling the Katnook Fields borehole cores. We thank B. Van de Moortele for his precious assistance during the TEM investigation. We also thank the anonymous reviewer for his constructive comments.

References

- Andreani, M., Gouze, P., Luquot, L., Jouanna, P., 2008. Changes in seal capacity of fractured claystone caprocks induced by dissolved and gaseous CO₂ seepage. *Geophys. Res. Lett.* 35, L14404.
- Andreani, M., Luquot, L., Gouze, Ph., Godard, M., Hoise, E., Gibert, B., 2009. Experimental study of carbon sequestration reactions controlled by the percolation of CO₂-rich brine through peridotites. *Environ. Sci. Technol.* 43, 1226-1231, doi: 10.1021/es8018429.
- Bachu, S.; Bonijoly, D.; Bradshaw, J.; Burruss, R.; Holloway, S.; Christensen, N.P.; Mathiassen, O.M. 2007. CO₂ storage capacity estimation: Methodology and gaps. *Int. J. Greenhouse Gas Control*, 1, 430-443.
- Baines, S. J.; Worden, R. H. *Geological storage of carbon dioxide* in "Geological Storage of Carbon Dioxide". (Geological Society, London, Special Publications, 233, 1-6, Baynes, S.J., Worden, R.H. (eds), 2004).
- Ballentine C. J., Schoell M., Coleman D., and Cain B. A., 2001. 300-Myr-old magmatic CO₂ in natural gas reservoirs of the west Texas Permian basin. *Nature (letter)* 409(6818), 327-331.
- Bickle, M., Chadwick, A., Huppert, H.E., Hallworth, M., Lyle, S., 2007. Modelling carbon dioxide accumulation at Sleipner: Implications for underground carbon storage. *Earth Planetary Science Letters*, 255, 164-176.
- Bickle, M. J. *Nature Geosci.* 2009, 2, 815-818.
- Chadwick, R.A., Noy, D., Arts, R., Eiken, O., 2009. Latest time-lapse seismic data from Sleipner yield new insights into CO₂ plume development. *Energy Procedia*, 1, 2103-2110.
- Chivas, A.R., Barnes, I., Evans, W.C., Lupton, J.E., Stone, J.O., 1987. Liquid carbon dioxide of magmatic origin and its role in volcanic eruptions. *Nature*, 326, 587-589.
- Damen, K., Faaij, A., Turkenburg, W. Health, Safety and Environmental Risks of Underground CO₂ Storage -Overview of Mechanisms and Current Knowledge, *Climatic Change* 2006, 74 (1-3): 289 - 318



- Daval, D., Martinez, I., Corvisier, J., Findling, N., Goffe, B., Guyot, F., 2009. Carbonation of Ca-bearing silicates, the case of wollastonite: Experimental investigations and kinetic modelling. *Chem. Geol.* 265, 63–78.
- de Marsily, G., 1981. *Hydrogéologie Quantitative*. Masson, Paris, 440 p.
- Druckenmiller, M.L., Maroto-Valer, M.M., 2005. Carbon sequestration using brine of adjusted pH to form mineral carbonates, *Fuel Processing Technology* 86 1599–1614.
- Giggenbach, W.F., Sano, Y., Schmincke, H.U., 1991. CO₂-rich gases from lake Nyos and Monoun, Cameroon; Laacher See, Germany; Dieng, Indonesia and Mt Gambier, Australia—variations on a common theme. *Journal of Volcanology and Geothermal Research*, 45 311–323.
- Goldberg, D.; Slagle, A. L. 2009. A global assessment of deep-sea basalt sites for carbon sequestration. *Energ. Procedia*, 1, 3675–3682.
- Golfier, F., Zarcone, C., Bazin, B., Lenormand, R., Lasseux, D., Quintard, M., 2002. On the ability of a Darcy-scale model to capture wormhole formation during the dissolution of a porous medium. *J. Fluid Mech.* 457, 213–254.
- Gouze, P., Luquot, L., 2011. X-ray microtomography characterization of porosity, permeability and reactive surface changes during dissolution. *J. Cont. Hydro.* 2011. 120–121, 45–55.
- Gunter, W. D.; Bachu, S.; Benson, S., *The role of hydrogeological and geochemical trapping in sedimentary basins for secure geological storage of carbon dioxide*, in "Geological Storage of Carbon Dioxide". (Geological Society, London, Special Publications, 233, 129–145, Baynes, S.J., Worden, R.H. (eds), 2004).
- Hangx, S. J. T.; Spiers, C. J. 2009. Reaction of plagioclase feldspars with CO₂ under hydrothermal conditions. *Chem. Geol.*, 265, 88–98.
- Hawkins, D. G. No exit: thinking about leakage from geologic carbon storage sites. *Energy* 2004, 29, 1571–1578.
- Hoefner, M.L., Fogler, H.S., 1988. Pore evolution and channel formation during flow and reaction in porous media. *AIChE J.* 34 (1), 45–54.
- Hoffert, M. I.; Caldeira, K.; Benford, G.; Criswell, D. R.; Green, C.; Herzog, H.; Jain, A. K.; Keshgi, H. S.; Lackner, K. S.; Lewis, J. S.; Lightfoot, H. D.; Manheimer, W.; Mankins, J. C.; Mauel, M. E.; Perkins, L. J.; Schlesinger, M. E.; Volk, T.; Wigley, T. M. L. Advanced Technology Paths to Global Climate Stability: Energy for a Greenhouse Planet. *Science* 2002, 298, 981–987.
- Hovorka, S. D., Doughty, Christine, Benson, S. M., Pruess, Karsten, Knox, P. R., 2004. The impact of geological heterogeneity on CO₂ storage in brine formations: a case study from the Texas Gulf Coast, in Baines, S. J., and Worden, R. H., eds., *Geological storage of carbon dioxide*: Geological Society, London, Special Publications, 233, p. 147–163.
- Kaszuba, J.P., Janecky, D.R., Snow, M.G., 2003. Carbon dioxide reaction processes in a model brine aquifer at 200°C and 200 bars: implications for geologic sequestration of carbon. *Appl. Geochem.* 18 (7), 1065–1080.
- Kaszuba, J.P., Janecky, D. R., Snow, M.G., 2005. Experimental evaluation of mixed fluid reactions between supercritical carbon dioxide and NaCl brine: Relevance to the integrity of a geologic carbon repository. *Chemical Geology*, 217(3–4) :277–293.
- Kelemen, P. B.; Matter, J. M. 2008. *In situ* carbonation of peridotite for CO₂ storage. *Proc. Natl Acad. Sci.*, 105, 17295–17300.
- Ketzer, J. M., Iglesias, R., Einloft S., Dullius J., Ligabue R., De Lima V. 2009 Water-rock-CO₂ interactions in saline aquifers aimed for carbon dioxide storage: Experimental and numerical modeling studies of the Rio Bonito Formation (Permian), southern Brazil *Applied geochemistry*, vol. 24, n°5, pp. 760–767.



- Kirste DM, Watson MN, Tingate PR. 2004. Geochemical modelling of CO₂-water-rock interaction in the Pretty Hill formation, Otway Basin. In: Boulton PJ, Johns DR, Lang SC (eds) Eastern Australasian basins symposium II. Special publication 19–22. Petroleum Exploration Society of Australia, Adelaide, South Australia, pp 403–411
- Kopsen, K.B., Scholten, T., 1990. Prospectivity of the otway supergroup in the central and western otway basin. Australian Petroleum Exploration Association Journal, 30 263-279.
- Lackner, K. S., 2003. A Guide to CO₂ Sequestration. *Science* 300, 1677–1678.
- Lasaga, A.C., 1998. Kinetic Theory in the Earth Sciences. Princeton University Press, New Jersey, 811 p.
- Luquot, L., Gouze, P., 2009. Experimental determination of porosity and permeability changes induced by injection of CO₂ into carbonate rocks. *Chem. Geol.* 265, 148–159.
- Matter, J. M.; Takahashi, T.; Goldberg, D. 2007. Experimental evaluation of *in situ* CO₂-water-rock reactions during CO₂ injection in basaltic rocks: Implications for geological CO₂ sequestration. *Geochem. Geophys. Geosyst.*, 8, Q02001.
- Matter, J. M.; Kelemen, P. B. 2009. Permanent storage of carbon dioxide in geological reservoirs by mineral carbonation. *Nature Geosci.*, 2, 837–841.
- Matthews, G.P., Ridgway, C.J., Small J.S., 1996. Modelling of simulated clay precipitation within reservoir sandstones. *Marine and Petroleum Geology* 13 (5), 581-589.
- O'Connor, W. K.; Dahlin, D. C.; Rush, G. E.; Gerdemann, S. J.; Nilsen, D. N. *Aqueous Mineral Carbonation: Final Report* DOE/ARC-TR-04-002 (US Department of Energy, 2004).
- Oelkers, E. H.; Gislason, S. R.; Matter, J. 2008. Mineral carbonation of CO₂. *Elements*, 4, 333–337.
- Pacala, S.; Socolow, R. 2004. Stabilization Wedges: Solving the Climate Problem for the Next 50 Years with Current Technologies. *Science* 305, 968–972.
- Palandri, J. L.; Rosenbauer, R. J.; Kharaka, Y. K. 2005. Ferric iron in sediments as a novel CO₂ mineral trap: CO₂-SO₂ reaction with hematite. *Appl. Geochem.*, 20, 2038-2048.
- Parker, K.A. 1992. The exploration and appraisal history of the katnook and ladbrooke grove gas fields, onshore otway basin, south australia. Australian Petroleum Exploration Association Journal, 32 :67-85.
- Parkhurst, D.L. *User's guide to PHREEQC-A computer program for speciation, reaction-path, advective-transport, and inverse geochemical calculations*, U.S. Geological Survey Water Resources Investigations Report, 1995, 95-4227, 143p.
- Perincek, D. and Cockshell, C.D. 1995. The otway basin : Early cretaceous rifting to neogene inversion. Australian Petroleum Exploration Association Journal, 35 :451-466.
- Prévot, M., Mankinen, E., Grommé, C., Lecaille, A., 1983. High paleointensities of the geomagnetic field from thermomagnetic studies on rift valley pillow basalts from the mid-Atlantic Ridge, *J. Geophys. Res.*, 88, 2316–2326.
- Rochelle, C. A.; Czernichowski-Lauriol, I.; Milodowski, A.E. *The impact of chemical reactions on CO₂ storage in geological formations: a brief review* in "Geological Storage of Carbon Dioxide". (Geological Society, London, Special Publications, 233, 87-106, Baynes, S.J., Worden, R.H. (eds), 2004).
- Rosenbauer, R.J., Koksalan, T., Palandri, J.L., 2005. Experimental investigation of CO₂-brine-rock interactions at elevated temperature and pressure: Implications for CO₂ sequestration in deep-saline aquifers. *Fuel Process. Technol.*, 86, 1581-1597.



- Savage, D., Cave, M.R., Haigh, D., Milodowski, A.E., and Young, M.E. 1993. The reaction kinetics of laumontite under hydrothermal conditions. *European Journal of Mineralogy*, 5, 523–535.
- Sheard, M.J., 1995. Quaternary volcanic activity and volcanic hazards. In: Drexel, J.F. and Preiss, W.V. (eds) *The geology of south Australia*. Vol. 2, Geological Survey of South Australia, Bulletin, 54, 264-268.
- Steefel, C. I.; Depaolo, D. J.; Lichtner, P. C. Reactive transport modelling: an essential tool and a new research approach for the earth sciences. *Earth Planet. Sci. Let.* 2005, 240, 539–558.
- Watson, M.N., Zwingmann, N., Lemon, P.R., N.M. Tingate 2003. Onshore otway basin carbon dioxide accumulations : Co₂-induced diagenesis in natural analogues for underground storage of greenhouse gas. *Australian Petroleum Exploration Association Journal*, pages 637-653.
- Watson, M. N., Boreham, C. J. & Tingate, P. R. 2004. Carbon dioxide and carbonate cements in the Otway basin: implications for geological storage of carbon dioxide. *APPEA Journal*, 703–720.
- Wigand, M., Carey, J.W., Schuett, H., Spangenberg, E., Erzinger, J., 2008. Geochemical effects of CO₂ sequestration in sandstones under simulated in situ conditions of deep saline aquifers. *Applied Geochemistry* 23(9): 2735-2745.
- Wilkinson, M., Haszeldine, R.S., Fallick, A.E., Odling, N., Stoker, S.J., Gatliff, R.W., 2009. CO₂-mineral reaction in a natural analogue for CO₂ storage – Implications for modeling. *Journal of Sedimentary Research*, 79, 486-494.
- Wolery, T.J. EQ3NR, a computer program for geochemical aqueous speciation-solubility calculations: Theoretical manual, user's guide and related documentation (Version 7.0). (Publication UCRL-MA-110662 Pt III, Lawrence Livermore Laboratory, Livermore, California, USA, 1992).
- Xu, T., Apps, J. A. & Pruess, K. 2004. Numerical simulation of CO₂ disposal by mineral trapping in deep aquifers. *Appl. Geochem.* 19, 917–936.
- Zerai, B., Saylor, B.Z., Matisoff, G., 2006. Computer simulation of CO₂ trapped through mineral precipitation in the Rose Run Sandstone, Ohio *Appl. Geochem.* 21, pp. 223–240.

Captions

Table 1: Structural formula of each individual mineral phase calculated from microprobe analyses.

Table 2: Brine composition for experiments KAT1 and KAT2.

Table 3: XRD and X-ray fluorescence analysis before and after experiment KAT2.

Fig. 1: Western Otway Basin (A) location of the Ladbroke Grove – Katnook analogue and nearby volcanic centres. The two fields are separated by a major fault (B).

Fig. 2: SEM image displaying the mineralogical composition and distribution of Katnook sample.



Fig. 3: Diagram of the experimental setup ICARE 2.

Fig. 4: Measured permeability (k in m^2) versus elapsed time.

Fig. 5: Normalized time-resolved concentrations of major cations during experiment KAT2.

Fig. 6: A: SEM image, realized on sample KAT2 after experiment, displaying laumontite, chamosite and albite dissolution. B: SEM image displaying microcline dissolution during CO_2 percolation experiment.

Fig. 7: SEM images of laumontite dissolution features and kaolinite precipitation.

Fig. 8: SEM images of kaolinite and silica precipitation on feldspar interface.

Fig. 9: pE-pH diagram. Phase distribution of the C-Fe-rich species as the function of pE and pH at $T = 95 \text{ }^\circ\text{C}$ and $P = 10 \text{ MPa}$ displaying the window where reduced carbon associated with magnetite is thermodynamically possible.

Fig. 10: TEM image of the chlorite fibres and precipitated magnesite surrounded by amorphous and poorly crystallized carbon. On the left: Chemical analysis associated with the TEM image, **a**: magnetite chemical analysis, **b**: carbon chemical analysis and **c**: chamosite chemical analysis. Raman spectra of precipitated carbon near chlorite compared with epoxy-resin spectra and disordered carbon spectra.

Fig. 11: Thermomagnetic curves (K - T curves) measured on the sample before (in black) and after (in grey) the percolation experiment. K - T curves at low and high temperature for Katnook sample are displayed. Measurements of thermal magnetic susceptibility changes are started by heating and ended by cooling.

Fig. 12: Total dissolved and precipitated mineral volumes versus elapsed time.

Fig. 13: Dissolved and precipitated minerals volumes for each mineral forming the Katnook sample versus elapsed time.

Fig. 14: Sketch illustration of laumontite, chamosite and feldspars dissolution and kaolinite precipitation explaining reactive surface and permeability decrease with time.

Figure in supplementary data: Normalized time-resolved concentrations of major cations during experiment KAT1.